研 究 解 説　　UDC 532.517.4 : 62

Turbulence Models for Practical Applications Part V
——Examples of Model Applications for 3D Flows——
乱流モデルの工学への適用　その5
——3次元流への適用例——

Wolfgang RODI* and Shuzo MURAKAMI**
W.ロ デ ィ・村 上 周 三

Examples are presented of calculations performed with the relatively simple turbulence models surveyed in the first half of paper (Part I[1], II[2]). The examples cover a wide range of engineering and environmental flows and are subdivided into two-dimensional thin-shear-layer flows[3], two-dimensional separated flows[4] and three-dimensional flows. In Part V, calculated results of three-dimensional flows are presented and the quality of the calculated results is assessed by comparison with measurements. The paper focuses on applications of the k-ε turbulence model and its variants, but, when available, results obtained with other models are included for comparison.

1. Introduction

In Part V, calculations are presented for flows that are strongly three-dimensional. The examples are restricted to incompressible flows without chemical reaction.

In general 3D flows involving reverse-flow regions, the original fully elliptic equations must be solved, at least locally, and this results in large storage and computing-time requirements. In most problems of this type, the numerical grid cannot be refined such that accurate, grid-independent solutions can be obtained with numerical schemes using upwind differencing. Higher-order methods appear to give significantly more accurate results, but for complex problems the grids that are practical on present-day computers are likely to be too coarse also when these schemes are used. A number of practically important 3D flows exist, however, that can be calculated with sufficient numerical accuracy. These are situations with a predominant flow direction, as they occur for example in ducts. These flows are of the shear layer type so that the originally elliptic 3D equations can be parabolised in the streamwise direction and an efficient marching-forward procedure can be used for their solution. Such procedures require only 2D storage so that relatively fine grids can be used, and since the streamlines are closely aligned with the grid lines in such flows, upwind differencing does not introduce significant numerical diffusion errors. The flows in ducts considered below are of this type.

*Visiting Scientist (University of Karlsruhe)
**Center for Development of Instrumentation Technology, Institute of Industrial Science, University of Tokyo

2. Duct and channel flows

Sharma[5] applied the standard k-ε model to calculate the flow in rectangular diffusors. Concentrating on the pressure recovery and on the influence of the inlet streamwise velocity distribution, he neglected the turbulence-driven secondary motions occurring in non-circular ducts. The simulation of these motions requires a more refined turbulence model, as will be discussed below. Sharma obtained fairly good agreement with measurements for the cross features of the diffusor situations considered.

In straight, non-circular ducts and open channels, secondary motions develop with velocities of the order of 2 to 3% of the mean longitudinal velocity. These motions are caused by the turbulent stresses and therefore often called turbulence-driven secondary motions. They cannot be predicted with an isotropic eddy viscosity model so that the standard k-ε model does not produce such motions. Rather, a model is necessary that simulates realistically the

anisotropic features of the turbulence and gives an accurate description of the Reynolds stresses. Both Reynolds-stress-equation models and algebraic-stress models have this capability. Demuren and Rodi[7] used an algebraic stress model to calculate the developing flow in a square duct with non-uniform inlet conditions. The flow situation is sketched in Fig. 1a. Developed flow in a square duct is subdivided at $x_1 = 0$ by a cruciform into four subchannels and the flow development in one of the subchannels is calculated, starting with developed flow conditions in the larger channel at $x_1 = 0$. This situation was a predictive test case for the Stanford Conference on Complex Turbulent Flows[6], i.e. the calculations were carried out before the measurements of Gessner (see 6)) were published. Fig. 1b compares the wall shear stress distribution along the cruciform wall at various downstream stations with measurements. The development from a strongly asymmetrical distribution to a symmetrical one is predicted very well. Fig. 1c shows the distribution of the streamwise velocity component along the corner bisector (see Fig. 1a) Again the development from an asymmetric profile to a symmetric one is well predicted. Fig. 1d displays the distribution of the velocity component U_2' along this sector, which is a measure of the secondary velocity. The shape of the secondary velocity distribution is predicted very well, while at the first two stations the magnitude is somewhat underpredicted. The distributions of the turbulent stresses reported in 7) agree also fairly well with the measurements. Fig. 1e shows how the secondary motion adjusts from a developed state in the larger duct with two counterrotating eddies in the lower left quadrant to developed flow in the subduct with eight eddies present. Without prior knowledge of experimental results, the model produced very realistic calculations for this complex flow.

Naot and Rodi[8] used a similar algebraic stress

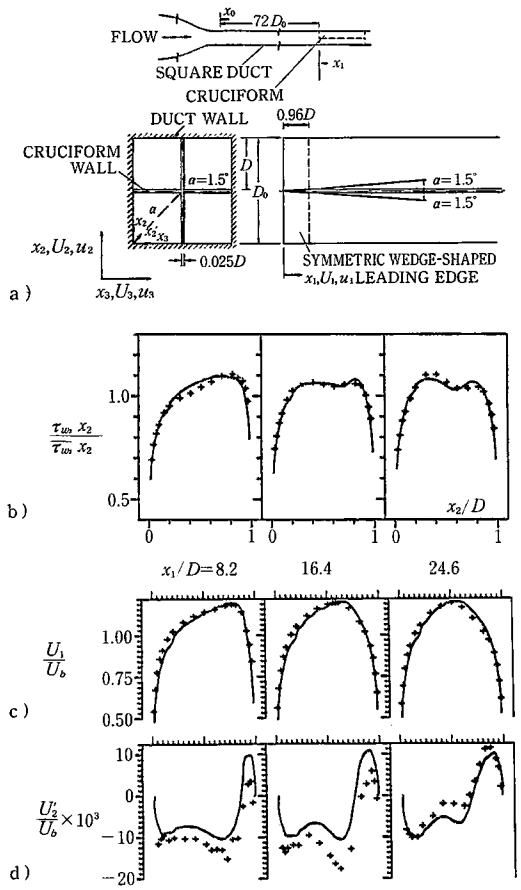

Fig. 1 Developing flow in a square duct with non-uniform inlet conditions (from 6) 7))
a) flow configuration
b) shear stress along crusiform wall
c) longitudinal velocity along corner bisector
d) secondary velocity along corner bisector

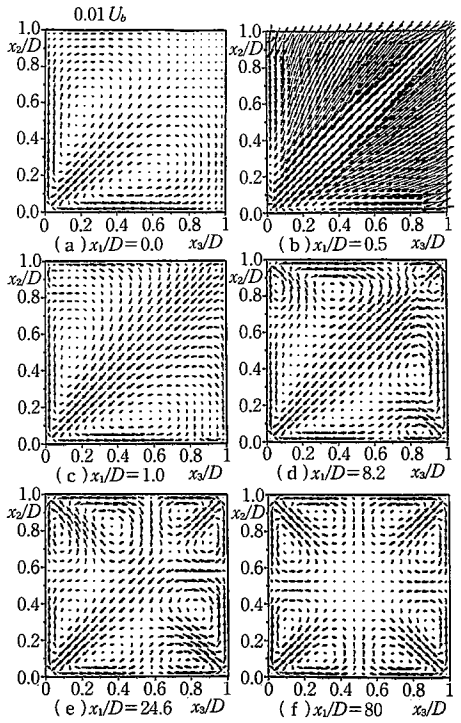

Fig. 1 e) development of secondary velocity

model to calculate developed flow in open channels with various width-to-depth ratios. One main difference to the model of Demuren and Rodi was the presence of a free surface correction term in the algebraic stress model. This caused the free surface to behave differently from a symmetry plane in closed channels. Figs. 2a and b show Naot and Rodi's[8] calculations of the axial velocity contours in the open channels studied experimentally by Raju[9] and Nikuradse[10]. The general features of the contours are predicted well in both cases, especially the depression of the velocity maximum below the free surface which is caused by the secondary motion. The contours in the lower part of Nikuradse's narrrow channel are not very accurately reproduced, and it appears that the secondary motion is overpredicted in the corner region leading to exaggerated bulging of the contours towards the corner. Fig. 2c compares Naot and Rodi's[8] predicted secondary velocity vectors for a channel of width-to-depth ratio 2 with the measurements of Nezu and Rodi[11]. In this case also, the measurements were performed after the calculations had been published, so that this is a real prediction. As opposed to the secondary motion in a quadrant of closed channel flow (see Fig. 1e), the secondary motion in open channel flow is no longer symmetrical to the diagonal. In the latter case, the upper vortex is much stronger than the lower one, also occupying a much larger area. This result of the calculation is in good agreement with the experimental observation.

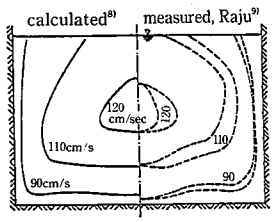

a) velocity contours for width to depth ratio of 1.5, measured contours are for 2 halves of channel, from 8)

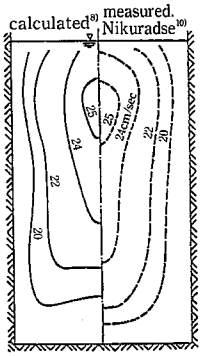

b) velocity contours for width to depth ratio of 0.6, from 8)

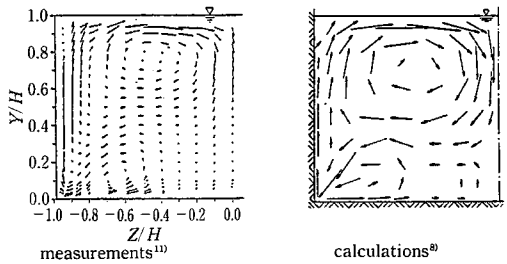

c) secondary velocity vectors for width to depth ratio of 2

Fig. 2 Developed open channel flow

Much stronger secondary motions can develop in curved channels and ducts, where they are not caused, however, by the turbulence but by the centrifugal forces acting at right angles to the main flow direction. Therefore, very accurate modelling of the turbulent stresses appears not necessary and hence the calculations presented below have been obtained with the standard k-ε model. Leschziner and Rodi[12] simulated the flow in the 180° open channel bend investigated experimentally by Rozovskii[13] Fig. 3a shows the geometry and compares the development of calculated and measured depth-average longitudinal velocity profiles, while Fig. 3b compares the variation of surface elevation along the inner and outer bank. As can be seen from Fig. 3a, the strong curvature results in a marked shift of the velocity maximum towards the inner bank as the flow enters the bend. Responsible for this shift is the acceleration due to the decrease in surface elevation near the inner bank and the deceleration near the outer bank caused by the increase in elevation at that bank. As the exit of the bend is approached, the reverse happens and the velocity maximum is shifted towards the outer bank. The calculated velocity vectors shown in Fig. 3c give a typical picture of the secondary motion. A detailed comparison of the calculated lateral velocity profiles with the experiments is presented in Fig. 3d. All the complex features of this flow discussed above are simulated correctly; the quantitative agreement with the experiments is not perfect but is certainly sufficient for practical purposes. It should be mentioned that, in this case, the agreement is not so much a merit of the turbulence model because the flow development is governed largely by pressure forces.

3. Buoyant jets into co-flowing channel flow

The next example concerns a coaxial heated water discharge into open channel flow. The discharge takes place over the full depth from a slot placed at

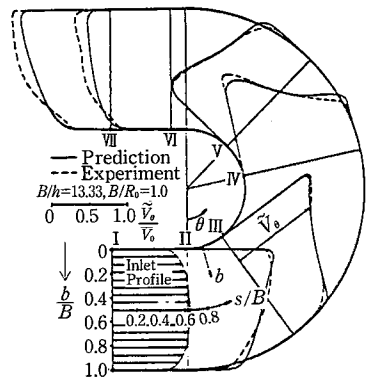

a) flow configuration and depth-averaged longitudinal velocity profiles

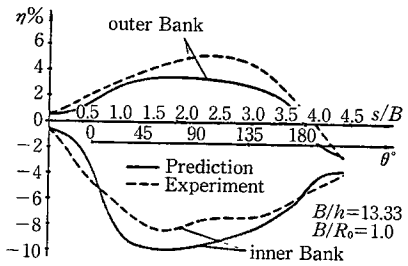

b) water-surface super-elevation at outer and inner banks

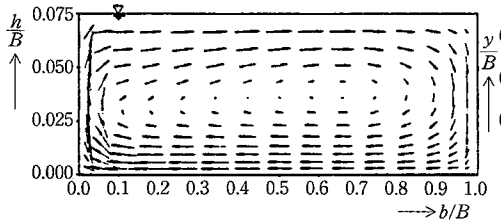

c) typical calculated secondary velocity field

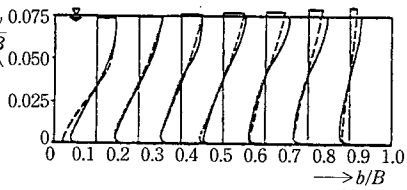

d) profiles of radial velocity at $\theta=102°$

Fig. 3 Flow in 180° open channel bend with $B/R_0=1.0$, $B/h=13.33$, calculations[12], measurements[13]

the channel center. The experimental situation simulated is characterised by a low densimetric Froude number ($F=3.3$) and a ratio of discharge to channel velocity of 1. Buoyancy effects are important both in the mean-flow equations and on the turbulence and have therefore to be accounted for in the turbulence model. Leschziner and Rodi[14] performed calculations of these flow situations with two variants of the k-ε model. The first variant employed the usual isotropic eddy viscosity relation and accounted for buoyancy effects solely by the buoyancy term in the k-equation (the constant $c_{3\varepsilon}$ in the ε-equaton was set to zero). The second variant is a local equilibrium version of the algebrlaic stress/flux model discussed in part I. The discharged warm water rises to the surface where it is deflected and spreads laterally. Due to continuity, cold ambient waters drawn towards the center near the bottom, and a secondary motion evolves as shown for a higher Froude number in Fig. 4a (calculations of 16) for $F=10$). The lateral surface spreading causes formation of warm-water pools off the center-plane, and the warm water lifts completely off the bottom to form a highly stratified shear layer. Fig. 4b shows by way of isotherms at three cross sections that both models reproduce the features discussed above fairly well. There is good quantitative agreement with the experiments to a distance of 8 slot widths from the discharge. At 16 slot widths, the agreement starts to deteriorate as the rising and lateral spreading of the warm water are somewhat underpredicted. What seems surprising at first is that, in spite of the presence of strong stratification, the two model variants give such similar results. The explanation is that in the algebraic stress/flux model effectively the eddy diffusivity for the vertical turbulent heat flux is reduced by the stratification, but since this in turn reduces the buoyancy-damping term in the k-equation, the net effect is fairly small.

4. Airflow in ventilated rooms

The next example also concerns a horizontal buoyant jet, but in this case with negative buoyancy and the jet being discharged into a room without any background velocity. For this reason, in this example (and in all examples to follow) no predominant flow direction exists and hence the original elliptic flow equations had to be solved. The calculations for this

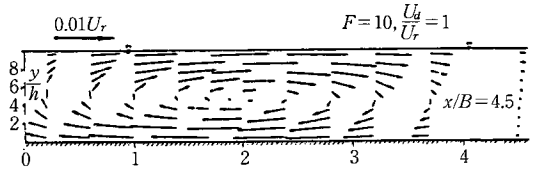

a) predicted secondary motion for $F=10$[16]

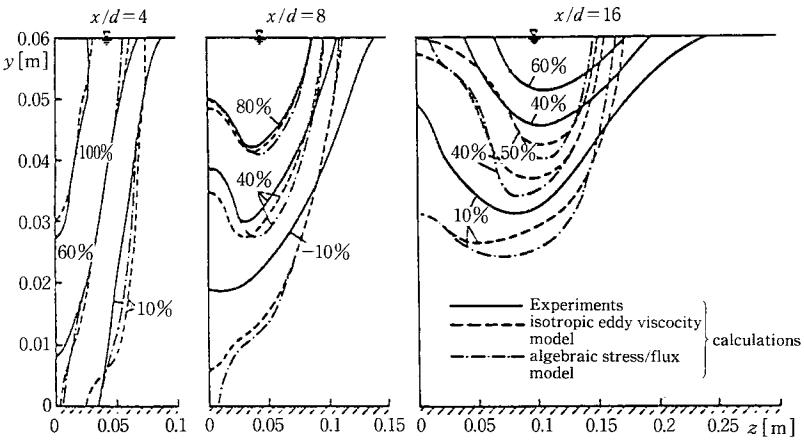

b) cross-sectional isotherms for $F=3.33$, calculations[14], measurements[15]

Fig. 4　Buoyant slot discharge into co-axial channel flow

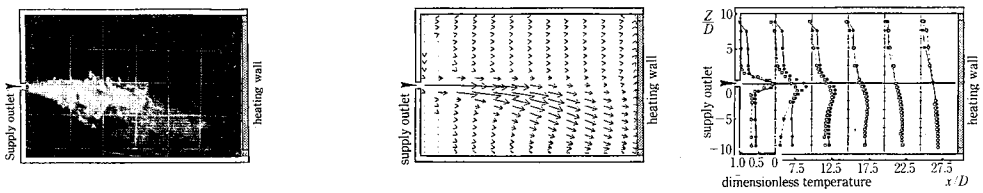

a) flow visualization　　b) calculated velocity vectors in vertical centre-plane　　c) measured and calculated temperature profiles in vertical centre-plane

Fig. 5　Negatively buoyant horizontal jet in room, from 17)

case have been performed by Nakagawa et al.[17] with the standard k-ε model. Fig. 5a, b gives an impression of the ensuing flow, i.e. the heavier jet discharged at the left at half room height sinking to the floor and the fluid leaving the room near the bottom. Fig. 5c compares calculations of the defect temperature profiles in the vertical centre-plane with measurements. This picture also shows clearly how the heavier jet sinks to the floor and indicates generally good agreement.

Murakami et al.[18][19] also performed 3D calculations with the k-ε model of the non-buoyant flow in a ventilated room with 4 inflow jets at the ceiling and 4 outlets in the corners near the bottom. In one test case[18], the room was empty, and the calculated and measured flow fields in the vertical plane through 2 of the discharge jets are compared in Fig. 6a. The jets discharging from the ceiling can be seen to impinge without much decay at the floor, causing recirculating flow between them. The calculated velocity field is in good agreement with the measured velocity vectors and the visualization picture. Fig. 6b compares calculated and measured contaminant concentration fields in the vertical plane through 2 of the jets. The concentration fields are due to a tracer at point (i). The calculated distribution corresponds well to the measured one. Although the calculated iso-concentration lines are not exactly the same as

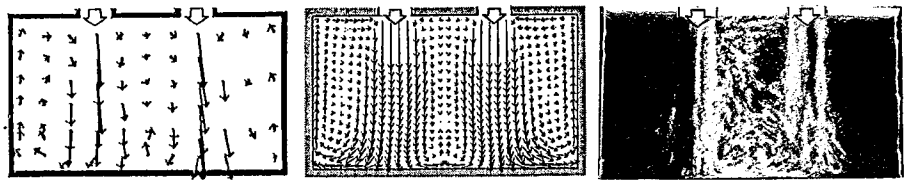

a) flow field

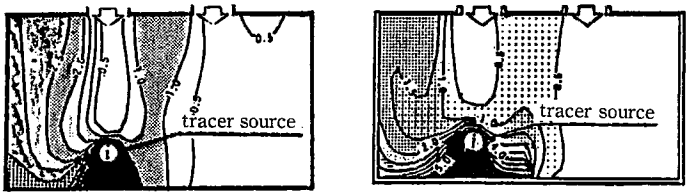

b) isolines of contaminant concentration for soure at point (i)

Fig. 6 Flow and contaminant concentration in ventilated empty room (without table), from 18)

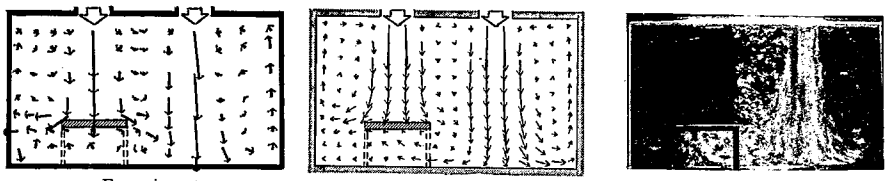

Fig. 7 Flow in ventilated room with table obstructing one of the descharge jets, from 19)

the measured ones, the main characteristics of the contaminant diffusion are well reproduced; the shape of the high concentration region under the tracer source, the low concentration region under the discharge hole, and the low concentration area on the opposite side where no tracer source exists.

Murakami and Kato[19] calculated a second test case in which one of the discharge jets had a table placed underneath its outlet. Fig. 7 shows how the flow is deflected by the table, and there is again good agreement between the calculated velocity field and the velocity measurements and visualization picture. The jet from the right supply outlet, under which no table is placed, is hardly affected by the table. Altogether, the studies of Murakami et al.[1819] have shown that the k-ε model is capable of simulating the flow in ventilated rooms with sufficient accuracy for engineering applications, at least for situations without significant buoyancy effects.

5. Discrete-hole film cooling

The cooling of gas turbine blades exposed to gas streams of very high temperature is affected often by discharging cooling air from discrete holes in the blade surface. The cooling air attaches to the surface providing a cooling film. A typical film cooling configuration with one row of holes is shown in Fig. 8a. The individual jets emerging from the discrete openings interact with the incoming flow, which is basically two-dimensional, generating thereby a strong three-dimensional flow field near the injection. For this situation, calculations with the standard k-ε model were performed by Demuren et al.[20] for various injection angles α, hole spacings s/D and blowing rates M (ratio of jet to cross-stream velocity). The film cooling effectiveness is characterised by the non-dimensional temperature

$$\eta=\frac{T_\infty-T}{T_\infty-T_j}$$

and Fig. 8b compares for $M=0.5$ and $\alpha=40°$ the calculated effectiveness averaged laterally between the holes with measurements[21]. The downstream development of this effectiveness and its dependence on the relative hole spacing can be seen to be predict-

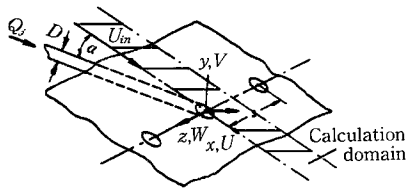

a) flow configuration

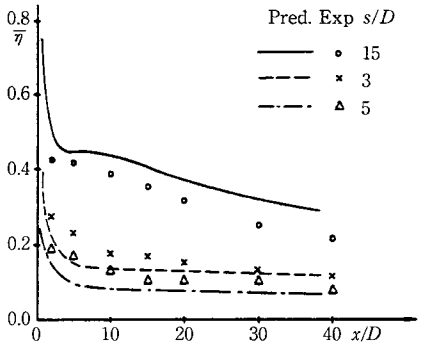

b) laterally averaged cooling effectiveness, $M=0.5$, $\alpha=45°$

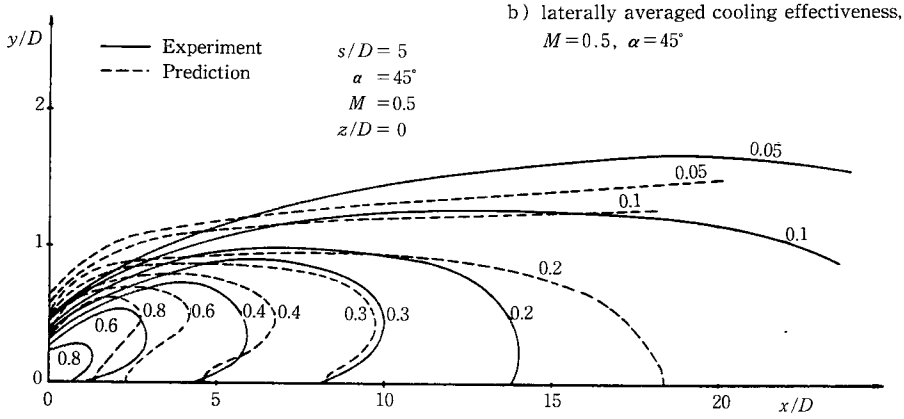

c) temperature contours $(T_\infty - T/T_\infty - T_j)$ behind an injection hole

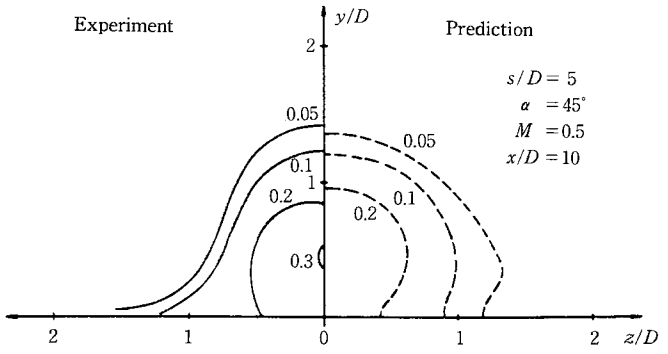

d) temperature contours $(T_\infty - T/T_\infty - T_j)$ in cross sectional plane $x/D=10$

Fig. 8　Film cooling by a row of jets; predictions[20], experiments[21]

ed quite well. Figs. 8c and d show that the three-dimensional nature of the flow is also reproduced fairly well by displaying respectively the isotherms at the centre-plane ($z=0$) and at a downstream cross-section ($x/D=10$) for one particular parameter situation. There is no perfect agreement about the details of the temperature distribution, but certainly the temperature field is predicted accurately enough for practical purposes. This shows that the k-ε model can be usefully employed also in such complex situations as multiple jets in a cross flow.

6. Flow past buildings

Fig. 9 compares calculated and measured velocity vectors reported by Murakami and Mochida[22] of the flow around a surface-mounted cube in a simulated atmospheric boundary layer. These calculations were carried out with the standard k-ε turbulence model.

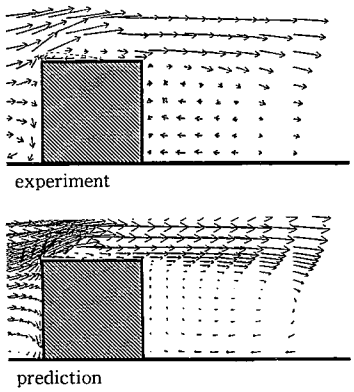

(a) pressure distribution on cube surface

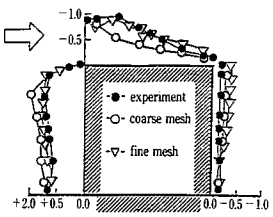

(b) from 22)

Fig. 9 Flow over surface-mounted cube; velocity vectors

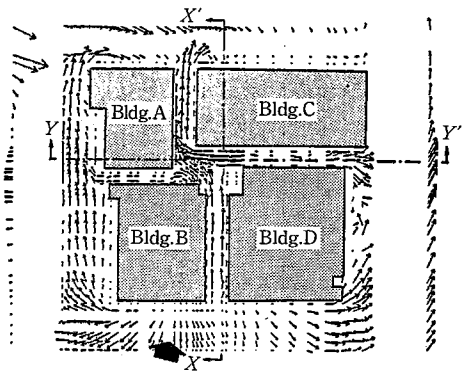

a) ground level (z=1.5m)

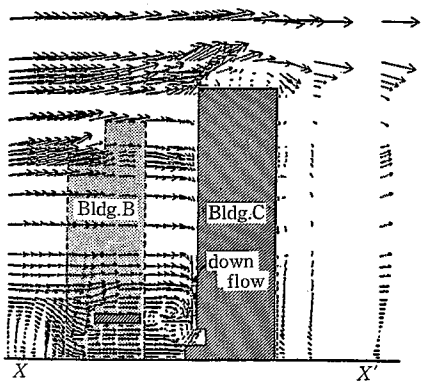

b) vertical plane at x-x'

Fig. 10 Predicted velocity vectors for flow over a group of buildings subjected to wind from SSW; from 23)

The velocity vector plots (Fig. 9a) clearly show a fairly large separation region behind the obstacle and smaller ones on its, top and front. There is generally good agreement between calculated and measured flow field, but the predictions overestimate somewhat the length of the recirculating flow region behind the cube. It should be mentioned that separation on the top of the cube was obtained only with a sufficiently fine numerical grid (non-uniform $50(x)\times49(y)\times28(z)$ grid). Fig. 9b compares calculated and measured pressure coefficients around the cube, including results obtained with a coarser grid ($45\times37\times21$) and the fine grid specified above. With the fine grid, the pressure distribution is well reproduced, except for that on the leeward side of the cube, where the predicted pressure is too high.

Murakami and Mochida[23] used the same calculation procedure to simulate the flow around a group of four buildings under construction. Fig. 10 a gives a top view of the four buildings, of which building A has 4 storeys, B has 15 storeys, C 20 storeys and D 7 storeys. The velocity vectors in Fig. 10 give an idea about the complicated flow field evolving in the case of the predominant wind from SSW. Near the ground (Fig 10a), a fairly strong wind can be seen to blow into the open space between buildings B and C. The velocity vectors in the vertical plane x-x' (Fig. 10b) indicate that a strong wind hits the windward surface of building C and diverges around the building, with a clear separation on the roof. Such calculations are probably of sufficient accuracy for estimating the wind effects in the design stage of buildings.

As a last example, the calculations of Demuren and Rodi[24] of the flow and plume spreading past a model cooling tower investigated experimentally by Viollet[25] are presented. These calculations were also carried out with the standard k-ε model. A non-buoyant situation is considered in which the fluid leaving the tower top carries a tracer whose distribution indicates the plume spreading and was measured in the experiments. Fig. 11 shows the calculated and measured velocity vectors and isoconcentration lines

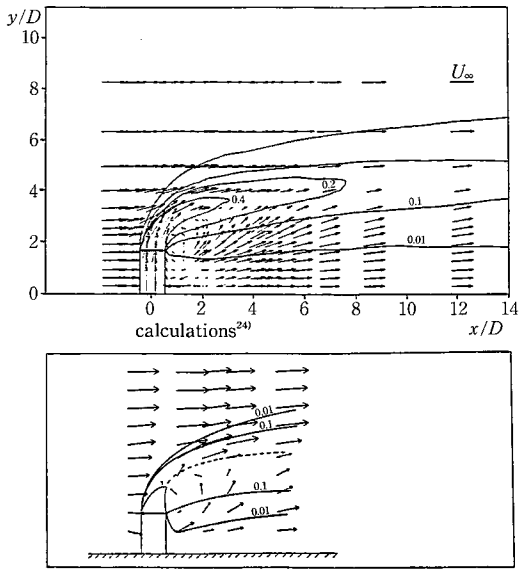

a) velocity vectors and isoconcentration lines in centre plane ($z=0$)

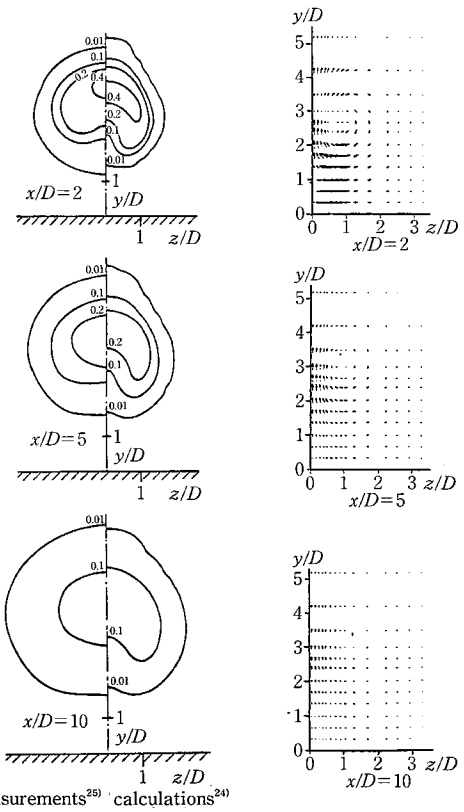

b) cross-sectional concentration contours

c) calculated secondary velocity vectors

Fig. 11 Flow and plume spreading past a cylindrical model cooling tower (from 24))

in the centre-plane through the tower ($z=0$). The velocity vectors indicate that a very complex flow field develops above and behind the tower, with two reverse flow regions, one behind the plume near the top of the tower and the other behind the tower itself near the floor. In the upper region behind the bending-over jet, the reverse flow seems to be stronger than near the ground, which may be caused by the jet entraining fluid from downstream. The upward velocity downstream of this reverse flow region is caused by the flow "filling" the wake behind the bending-over jet. This upward motion is strengthened by the longitudinal vortex generated by the bending-over jet as shown in Fig. 11c. Even though there may not be agreement in all the details, the calculated velocity field can be seen to be very similar to the measured one. The concentration field appears also to be in reasonable agreement. The development of this field in cross-sectional planes is shown further in Fig. 11b, where calculated and measured isoconcentration contours are compared for three downstream stations. The distortion of the isoconcentration lines to kidney shape is caused by the longitudinal vortices generated behind the tower, as indicated by the secondary velocity vectors shown in Fig. 11c. The kidney-shaped behaviour appears to be somewhat overpredicted by the model, indicating that the calculated longitudinal-vortex motion is somewhat too strong. On the whole, however, the plume spreading and dilution is very well predicted by the model. The $63\times31\times32$ grid in the x-, y- and z-directions is certainly still too coarse to resolve all the details of the very complex flow in the vicinity of the tower. Also, the grid was rectangular so that the circular tower geometry had to be approximated by steps. Further testing of the k-ε model for such complex situations certainly requires a more refined numerical treatment.

7. CONCLUSION REMARKS

For three-dimensional flow situations, the standard k-ε model appears to yield satisfactory results for straight and curved duct flows in which the turbulence-driven secondary motion is not essential. When this motion is important, the standard model fails, but algebraic stress models appear to simulate this motion in both closed non-circular ducts and open

channels quite well, and there is no evidence that stress-equation models give significantly better results for such flows. Buoyancy effects are also well reproduced by the algebraic stress models. In certain cases, the simpler isotropic eddy viscosity model (using a constant c_μ) seems sufficient when the buoyancy production/destruction term in the k-equation is included. Further testing is necessary to find out in which cases this simpler treatment is possible. For the most complex flows considered, i.e. 3D air flows in rooms, jets in a cross flow and the flow around buildings, the k-ε model appears to give reasonable results that may suffice for practical purposes even though they are not always very accurate. The turbulence-model performance is difficult to judge in these complex situations because detailed experimental information is often not available, but also because the numerical accuracy that can be obtained is somewhat questionable, particularly when the upwind differencing scheme is used. In these situations, the limits of the computers available to most users today are reached quickly.

ACKNOWLEDGEMENTS

This paper was initiated while the first author (WR) was a guest at the Institute of Industrial Science of the University of Tokyo; he should like to express his deep gratitude for the overwhelming hospitality received during his stay at the Institute.

(Manuscript received, December 6, 1989)

REFERENCES

1) Rodi, W., Shuzo, M. "SEISAN-KENKYU" Vol. 41, No. 8, 1989. 8.
2) Rodi, W., Shuzo, M. "SEISAN-KENKYU" Vol. 41, No. 9, 1989. 9.
3) Rodi, W., Shuzo, M. "SEISAN-KENKYU" Vol. 41, No. 12, 1989. 12.
4) Rodi, W., Shuzo, M. "SEISAN-KENKYU" Vol. 42, No. 1, 1990. 1.
5) Sharma, D., Ph. D. thesis, University of London, 1974.
6) Kline, S.J., Cantwell, B. and Lilley, G.M., Eds., Proc. 1980-81 AFOSR-HTTM Stanford Conference on Complex Turbulent Flows, 1982.
7) Demuren, A.O. and Rodi, W., Computers and Fluids, Vol 15, 1987, 47-57.
8) Naot, D. and Rodi, W., ASCE J. Hydraulics div., Vol. 108, No. HY 8, 1982, pp. 948-969.
9) Raju, J., by Kirchner, Die Wasserwirtschaft, Stuttart, 39. No. 8, 1949, pp. 137-142 and 168-174.
10) Nikuradze, J., Forschungsarbeiten, Heft 281, 1926, pp. 36-44.
11) Nezu, I. and Rodi, W., Proc. 21st IAHR Congress, Melbourne, Australia, August 1985.
12) Leschziner, M.A. and Rodi, W., J. of the Hydraulics Div., ASCE, Vol. 105, No. HY 10, 1979, pp. 1297-1314.
13) Rosovskii, I.L., published by the Academy of Sciences of the Ukrainian SSR, Kiev-printed in Jerusalem by S. Monson, 1975.
14) Leschziner, M.A. and Rodi, W., ASCE J. of Hydraulic Engg., Vol. 109, No. 10, 1983, pp. 1380-1385.
15) Rodi, W. and Weiss, K., ASCE J. Hydraulics Div., Vol. 108, No. HY6, 1982, pp. 737-746.
16) Rastogi, A.K. and Rodi, W., J. of the Hydraulics Div., ASCE, No. HY3, 1978, pp. 397-420.
17) Nakagawa, H., Murakami, S. and Kato, S., Summaries of Technical Papers of Annual Meeting, Architectural Institute of Japan, 1988 (in Japanese).
18) Murakami, S., Kato, S. and Suyama, Y, ASHRAE Transaction 1987, Vol. 93, Part 2.
19) Murakami, S. and Kato, S., Building and Environment, Vol. 24, No. 1, 1989, pp. 51-64.
20) Demuren, A.O., Rodi, W. and Schönung, B., Journal of Turbomachinery, Vol. 108, 1986, pp. 124-130.
21) Kruse, H. and Metzinger, H., DFVLR Köln, Internal Report, IB 325-9-84, 1984.
22) Murakami, S. and Mochida, A., Journal of Wind Engineering and Industrial Aerodynamics, Vol. 31, 1988, 11 (in press).
23) Murakami, S. and Mochida, A., Building and Environment, Vol. 24, No. 1, 1989, pp. 85-98.
24) Demuren, A.O. and Rodi, W., ASME Journal of Heat Transfer, Vol. 100, 1987, pp. 113-119.
25) Viollet, P.L., Dissertation, Université Pierre et Marie Curie, Paris, 1977.